drones

MDPI

Review

Ice Accretion on Fixed-Wing Unmanned Aerial Vehicle—A Review Study

Manaf Muhammed * and Muhammad Shakeel Virk

Arctic Technology & Icing Research Group, UiT—The Arctic University of Norway, 8514 Narvik, Norway; muhammad.s.virk@uit.no

* Correspondence: manaf.muhammed@uit.no; Tel.: +47-98863857

Abstract: Ice accretion on commercial aircraft operating at high Reynolds numbers has been extensively studied in the literature, but a direct transformation of these results to an Unmanned Aerial Vehicle (UAV) operating at low Reynolds numbers is not straightforward. Changes in Reynolds number have a significant impact on the ice accretion physics. Previously, only a few researchers worked in this area, but it is now gaining more attention due to the increasing applications of UAVs in the modern world. As a result, an attempt is made to review existing scientific knowledge and identify the knowledge gaps in this field of research. Ice accretion can deteriorate the aerodynamic performance, structural integrity, and aircraft stability, necessitating optimal ice mitigation techniques. This paper provides a comprehensive review of ice accretion on fixed-wing UAVs. It includes various methodologies for studying and comprehending the physics of ice accretion on UAVs. The impact of various environmental and geometric factors on ice accretion physics is reviewed, and knowledge gaps are identified. The pros and cons of various ice detection and mitigation techniques developed for UAVs are also discussed.

Keywords: atmospheric icing; UAV; LWC; MVD; Reynolds number; aerodynamic penalties; IPS; modal analysis

Citation: Muhammed, M.; Virk, M.S. Ice Accretion on Fixed-Wing Unmanned Aerial Vehicle—A Review Study. *Drones* **2022**, *6*, 86. https://doi.org/10.3390/drones6040086

Academic Editors: Andrzej Łukaszewicz, Wojciech Giernacki, Zbigniew Kulesza, Jaroslaw Pytka and Andriy Holovatyy

Received: 28 February 2022
Accepted: 20 March 2022
Published: 28 March 2022

1. Introduction

UAV is an aircraft without an onboard human pilot. The main components of a UAV are the aircraft structure, ground control center (remote), payload (camera), and a data link for the communication between aircraft and ground control center [1]. According to their structure, UAVs are classified into four broad categories: *fixed-wing UAVs*, *rotary-wing UAVs*, *flapping-wing UAVs*, *and blimps* [2]. The smallest UAVs operate at less than 1200 feet above ground level, while the largest can fly up to 60,000 feet. The size and cost of UAVs vary according to application, ranging from pocket-sized micro-UAVs to large UAVs comparable in size to passenger aircraft. Even though crew safety is not a primary concern for UAVs due to their unmanned nature, but due diligence must be exercised in the design and manufacture of UAVs to avoid any financial losses. Historically, UAVs were used exclusively for military and defense purposes. However, over the last decade, UAVs have demonstrated their potential for use in various civil and public safety applications, including mapping, surveying, and photography. In 2021, a German marketing consultancy reported that UAVs have been used in 237 different applications [3]. As per the Unmanned Aircraft System Roadmap 2005–2030 [4], currently, more than 250 models of UAVs are manufactured globally by 32 nations.

With an increase in human activity in ice-prone high north regions, the use of UAVs has increased as well, with potential applications including ice reconnaissance, determining sea-ice thickness, surface roughness, and surface temperature over ice, water, and land, retrieving the spectral albedo of land surfaces, and monitoring coastal erosion [5]. UAVs also play a critical role in emergency and catastrophe scenarios in cold regions [6]. In addition,

UAVs can help ships to navigate safely by detecting icebergs. Arctic regions can serve as a showcase for UAVs to demonstrate their capabilities in light of the global climate change scenario. However, for optimal and safe UAV operation in ice-prone regions, ice accumulation on its structure is a significant safety problem. Icing is considered as one of the predominant causes of aircraft loss of control [7]. Three General Atomics MQ-1 Predator UAVs of the US military were crashed in Afghanistan in 2001 and 2002 due to icing hazards. The US military's Northrop Grumman Global Hawk UAV crashed due to icing during the Enduring Freedom operation in Afghanistan [8]. Military UAV missions have frequently been aborted due to inclement weather, which significantly impacts the mission's success [9]. For example, icing prevents Hunter UAV flights from October to April in Kosovo [10]. As a result, there is a growing need for a thorough understanding of ice accretion physics and the development of ice mitigation measures to ensure the safe operation of UAVs in icing conditions.

The operation of UAVs in high north regions is prone to three main challenges: low temperature, high wind speeds, and atmospheric icing. Some materials can become brittle at low temperatures and develop cracks due to expansion and contraction. Additionally, batteries lose their capacities in low temperatures and thus reduce the range and endurance limits of a UAV flight. The lithium-ion battery used in UAVs is more sensitive to low temperatures [11]. UAVs have a lower flight speed, lighter takeoff weight, smaller size, and lower flight altitude than manned aircraft, so these factors make UAVs more susceptible to wind disturbance compared to manned aircraft [12]. High wind speeds challenge the stability of small UAVs operating at a velocity less than 20 m/s. It can lead to loss of control and trajectory excursions resulting in a crash. Atmospheric icing can be considered the most dangerous hazard for UAVs operating in high north regions (See Figure 1). The ice accretion along a UAV structure causes deterioration of aerodynamic performance and structural characteristics leading to catastrophic failures. Atmospheric icing occurs when the super cooled water droplets freeze into ice upon impingement on a surface. In-cloud icing on structures are mainly classified into rime, glaze, and mixed ice. Glaze ice can result in the formation of complex ice structures like horns, large feathers, and "lobster tail like structures", and are therefore considered as the most dangerous icing condition.

Figure 1. Ice accretion on fixed-wing UAV [13,14].

UAVs are more prone to icing than conventional manned aircraft for the following reasons: (1) The presence of supercooled water droplets is pervasive in the lower 10 km of the atmosphere. Above 10 km, the concentration of supercooled water droplets decreases due to the extremely low temperature (>−45 °C) and low liquid water content [15]. As most UAVs fly in the lower atmosphere, they are more susceptible to ice accumulation than manned aircraft [16]. The high-altitude UAVs flying above 10 km must still pass through the icing layers during takeoff and landing and are also prone to icing effects. (2) UAVs operating at lower velocities than conventional aircraft have prolonged exposure to icing environments. (3) Manned aircraft operate with ice mitigation systems, but most UAVs operate without any ice protection systems because of their weight and power constraints.

(4) Composite materials used in the manufacturing of UAVs have lower thermal conductivity than the conventional metal-based airframes used for manned aircraft. Thus, the rate of heat transfer and dissipation of latent heat of fusion released during solidification is much slower for composite materials. It results in severe water runback and the formation of complex rivulet-like ice structures on the surface of UAVs [17]. (5) Low Reynolds number airfoils are so sensitive that even small changes on the surface of the main lifting element could significantly impact its performance. Thus, ice accretion on unmanned aerial vehicles (UAVs) must be studied separately from that on manned aircraft to understand the icing characteristics better and propose appropriate ice detection and mitigation measures.

Ice accretion can deteriorate the aerodynamic performance, structural integrity, and aircraft stability. Several studies can be found in the literature investigating the aerodynamic performance of aircraft under icing conditions [18]. In the last couple of decades, similar studies were also done for UAVs. Ice accretion on the UAV can alter its weight, which in turn changes its center of gravity and thus causes a deterioration of the performance and stability of aircraft [19]. Thus, proper ice mitigation techniques need to be implemented to avoid performance losses due to ice accretion.

2. Methods of Studying Ice Accretion on a UAV

Atmospheric icing research was mainly focused on the ice accretion problems in large Reynolds number applications like manned aircraft and the icing on structures like wind turbines, power networks, and so on [18–23]. The study of ice accretion on UAVs has gained interest only from the beginning of the 21st century and only a few researchers have worked in this field of science. One of the earlier works for icing on UAVs was published by Siquig in 1990 [16]. This can be considered a first reported work that discusses the ice accretion characteristics and related aerodynamic consequences of UAVs explicitly. The operational challenges of different UAVs under icing conditions and the need for better forecasting techniques are discussed. Ice accretion on a UAV can be studied using four different methodologies: (1) Analytical methods (2) Field measurements (3) Lab experiments (4) Numerical simulation.

2.1. Analytical Modelling

An analytical expression for studying the ice accretion on structures was formulated by Finstad et al. in 1986 [24]. Even though this analytical model is used to study aircraft icing, it is based on her works about ice accretion on the cylinder and therefore cannot be used directly for the icing on UAVs. Another analytical model suitable for the ice accretion on UAVs was derived by Szilder et al. in 2011 [25]. This model was based on the conservation of mass and energy for the impinging, flowing, and freezing droplets on the surface of the airfoil, and it relates the atmospheric temperature (T_∞) and Liquid Water Content (LWC) for a specified Reynolds number (Re), Median Volume Diameter (MVD) and runback limit.

2.2. Field Measurements

Field measurements based on actual flight tests are the most accurate way to study the ice accretion process. But these tests are costly and need constant monitoring and waiting for the desired operating conditions. Only a few such studies are available in the open literature for fixed-wing UAV icing. Avery [26] in 2013 performed flight testing of a small UAV to characterize the atmospheric icing environments. In 2016, Williams et al. [27] tested the Kahu-Hawk UAV's aerodynamics and flight stability. Before the flight, prefabricated ice shapes were glued to the wing's leading edge. Similar studies were done by Matiychyk et al. [28] in 2019 on a UAV M-10-2 "Oko". In contrast to the previous study, ice was naturally allowed to accrete on the UAV. Ice deposits were observed along the wing's full length leading edge, the tail unit's leading-edge, on the front surfaces of the pitot-static tube and video antennas. An ice thickness of 1.5 mm was observed on the wing leading edge. The performance parameters were obtained with the help of a Mode of Flight Recorder (MFR), and it was observed that the drag force increased about 40% due to icing.

The increase in the drag force increased the power requirement by 10%, and thus, the average index of the battery rose from 25.5 A to 35 A. In 2021, Siddique [29] performed inflight testing of a Sonicmodell Skyhunter fixed-wing UAV at three different flight conditions of calm, windy, and icing conditions at the Iowa State University's Bio Century Research Farm (BCRF). The T_∞ value observed during the icing condition test was −1.5 °C and it leads to glaze ice formation on all leading edges and propellers. Water runback rivulets were visible on the top surface of the wing downstream of the leading edge. The propellers were heavily iced, leading to the formation of horns and ridges on pressure and suction sides. A dramatic increase in power requirement of 240% was observed during the ice accretion compared to calm weather conditions, leading to more battery power consumption.

2.3. Lab Experiments

Two major lab-based experimental techniques are employed to study the ice accretion phenomenon: Icing wind tunnels and cold room experiments. Icing wind tunnels are like standard wind tunnels with an additional cooling system to maintain the low temperatures and a spray system to inject water droplets into the airflow prior to entering the tunnel test section. The use of such icing wind tunnels allows for the prediction of ice shapes along with the measurement of aerodynamic loads and forces [30]. In 1944, NASA built the Icing Research Tunnel (IRT) at the Lewis Flight Propulsion Laboratory in Cleveland, Ohio. Several icing experiments were then conducted to understand the effect of ice accretion on the aerodynamic performance of aircraft [31,32]. However, most icing wind tunnels operate without a force balance measure system and therefore can only be used to trace ice shapes, but the ability to provide performance data is limited. NASA IRT [33], Boeing ice wind tunnel [34], altitude icing wind tunnel research facility in Canada [35], Braunschweig icing wind tunnel [36], Cranfield University icing wind tunnel [37], and CIRA ice wind tunnel in Italy [38] are some typical ice wind tunnels around the world. Cold room experiments are carried out in refrigerated cold rooms or outdoors in cold climates. A spray system located in front of the test vehicle creates the icing cloud. The major drawback of these rooms is their low operating velocity and they are often quite large in size [39]. Experiments on lab facilities did not offer the necessary precision and accuracy in simulating the icing conditions expected to be found in nature. A detailed discussion about the similarity parameters and scaling laws considered during lab based icing studies can be found in [40].

2.4. Numerical Simulation

Numerical icing simulations have four major modules: (1) Aerodynamic simulations for air flow field determination, (2) Determination of water droplet trajectories using a droplet impingement solver, (3) Ice growth process using a thermodynamic model, and (4) Remeshing module. Potential flow or Navier-Stokes stokes-based solvers are used for flow field determination and the Eulerian or Lagrangian approach is used to determine droplet trajectories. The thermodynamic solvers of most existing ice growth solvers are based on the Messinger model [41]. A detailed description of the physics involved in these processes can be found in [18]. Atmospheric parameters like wind speed, ambient temperature, Liquid Water Content (LWC), Median Volume Diameter (MVD), or droplet size distribution and duration of the icing event need to be supplied as an input to the numerical solver. The typical ice accretion modeling tools include LEWICE based on a 2D panel method developed by NASA Lewis Research Center [42], ONERA 2D/3D governed by Euler equations developed by ONERA in France [43,44], IMPIN3D developed by CIRA, Italy [45], CANICE based on the panel method developed by Bombardier Aerospace and Ecole Polytechnique de Montreal, Canada [46], MORPHICE based on the morphogenetic ice accretion model [47], and the second-generation 3D icing simulation system FENSAP-ICE based on Reynolds-Averaged Navier-Stokes developed by Newmerical Technologies International, Canada [48,49].

Icing tunnel experimental results are only available for the high Reynolds number applications in the past. The paucity of low Reynolds number investigations hinders the

validation of numerical ice accretion prediction codes for low Reynolds number applications like ice accretion on UAVs. Therefore, such validations were performed in the past by comparing the numerical predictions with the available lowest Reynolds number test results. Szilder et al. in 2011 performed the validation of his numerical icing code based on the morphogenetic ice growth model (MORPHICE) at low Reynolds number by comparing its predictions with the results of icing tunnel test studies done on NACA 0012 airfoil at $Re = O(10^6)$ [50,51]. Following Szilder's work, Hann et al. [52] in 2018 also used the same experimental results to validate FENSAP ICE and LEWICE codes as a part of his ice accretion studies on UAVs. The ice shapes predicted by icing tunnel tests and numerical simulations vary greatly. The numerical codes underpredicted ice thickness, and the icing extents are more than experimental predictions. Thus, the validation of the existing numerical codes at low *Re* remains as a knowledge gap in the scientific literature.

To cover this gap, Williams et al. in 2017 [27] performed experimental studies on RG-15 airfoil at the NRC Altitude Icing Wind Tunnel (AIWT), Canada. The icing test was performed for a continuous maximum and an intermittent maximum icing condition as per FAR 25 Appendix C atmospheric icing envelope [53]. Glaze ice was observed for $T_\infty = -5$ °C and rime ice characteristics were observed at $T_\infty = -20$ °C. Later Richard Hann of the Norwegian University of Science and Technology (NTNU), Norway conducted three major experimental campaigns to generate the ice shapes data for UAV airfoils at low Reynolds number. In spring 2019, Hann [54] performed experiments on RG-15 and NREL S826 airfoil at the Cranfield icing wind tunnel. Ice conditions were chosen to generate three different icing morphologies of glaze, mixed, and rime for Reynolds number in the order of 10^5. The studies implemented and discussed two novel methods to capture the ice shapes in experiments: 3D scanning and photogrammetry. Numerical icing simulations were performed using FENSAP-ICE and LEWICE to validate the results, but there was a significant difference in the prediction of ice shapes. In fall 2019, Hann et al. [55,56] again performed icing studies on RG15 airfoil at the icing wind tunnel of the Technical Research Centre of Finland (VTT). The experiments were done for the glaze and mixed ice conditions to obtain the ice shapes as shown in Figure 2. In 2020, he [57] extended his experimental studies to NREL S826 airfoil for three different icing conditions of glaze, mixed, and rime ice respectively as shown in Figure 3.

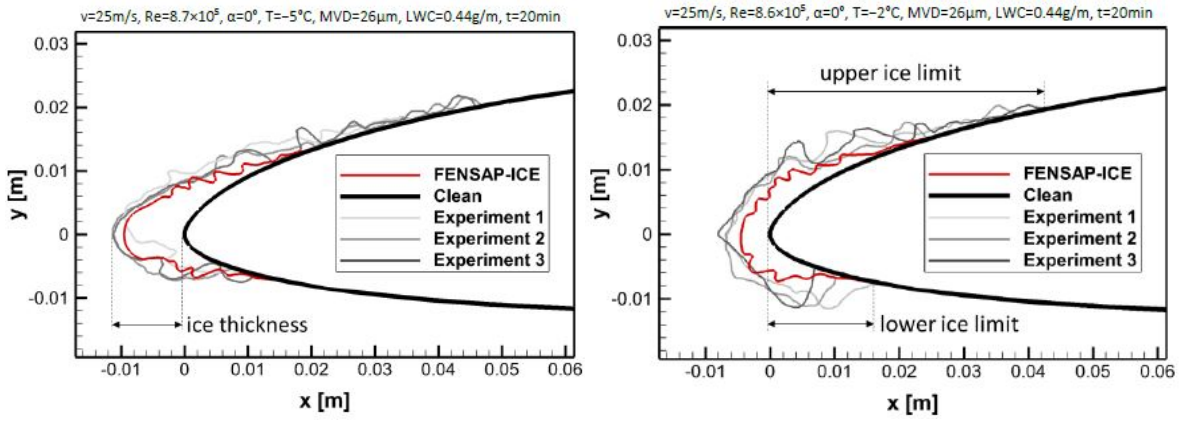

Figure 2. Experimental ice shapes on RG-15 airfoil [56].

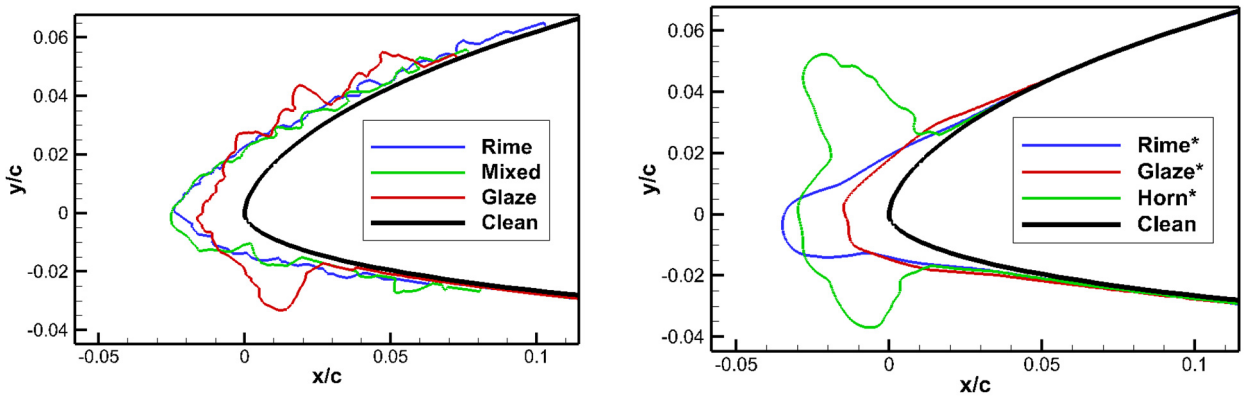

Figure 3. Ice shape predicted by (**a**) experiments and (**b**) numerical codes on NREL S826 airfoil [57]. These simulated ice shapes are marked with an asterisk to distinguish them from the experimental shapes.

Numerical ice accretion studies on UAVs have been performed by researchers primarily using three major icing codes: MORPHICE, LEWICE, and Ansys FENSAP-ICE. The validation of MORPHICE at low Reynolds number ($<O(10^5)$) is not reported in open literature at the time of writing this review paper. Hann et al. validated the LEWICE and FENSAP-ICE ice codes by comparing their predictions with the results of his icing tunnel tests [56]. Additionally, Hann compared the performance of these codes in predicting the ice accretion on NACA 0012 and NREL S826 airfoil [52]. Overall, the predictions for the rime ice conditions are better than the glaze ice, and the FENSAP ICE predictions were closer to the experimental results. However, the numerical codes underpredict the ice thickness and the ice limits, especially on the suction side. The ice shape predicted by LEWICE is smooth, in contrast with the rugged ice surface in experimental results. For glaze ice, the predictions of the FENSAP ICE validate with the experiments better than the LEWICE predictions. This may be because of the limitations of the panel method in predicting the complex flow behaviors, but on the other hand, FENSAP ICE based on the Navier stokes equation showed higher accuracy.

These validation studies indicate the capability of existing numerical icing codes to predict the ice shapes for different meteorological conditions. Overall, the numerical codes can reliably predict the rime ice accretions but fall short of accurately predicting glaze ice due to the intricate physics involved. Kind et al. [40] also made a similar observation for ice accretion studies on manned aircraft. The difference in the ice shape predicted by numerical codes and experiments can be attributed to the numerical model's limitations or experimental uncertainties. Experimental uncertainties mainly include the limitation of existing techniques and the possibility of errors and some of them are listed here. (1) Ice accretion is a dynamic process, and the shape of the accreted ice keeps on changing with time. Therefore, the ice shapes obtained by manual tracing correspond to the ice shape at a particular instant of time. So advanced ice shape tracing techniques need to be developed to get the ice shape at various time instants. (2) Proper calibration of LWC and MVD with accurate droplet distribution is necessary to obtain more realistic experimental conditions. (3) The ice density variability during tunnel simulations is another challenge for experiments [54]. (4) The ice accretion is usually obtained for a fixed value of angle of attack, but the angle of attack keeps on changing during the actual flight trajectory. (5) The assumption of the infinite wing concept in most studies also limits the accuracy by restricting the flow dimensions to 2D. (6) The spatial and temporal variability of the ice accretion test results is another phenomenon that questions the accuracy of icing tunnel tests [51]. (7) When tests are conducted on a sub-scale model, dynamic similarity parameters for the airflow, droplet trajectories, and thermodynamic freezing process must be satisfied, but it is difficult to achieve in practice. Numerical models are usually built

based on various simplifications and assumptions, and there is always a question of the validity of the numerical models used. Unlike the fluid flow simulation, ice accretion modeling includes coupling of a fluid flow solver, droplet trajectory module, and heat transfer module. Thus, there are approximations at all three stages, which can considerably affect the accuracy of the results. In addition, the accurate modeling of the boundary layer, roughness effects, and the turbulent flow characteristics need to be considered. Additionally, the existing numerical techniques and associated models are developed for ice accretion at a high Reynolds number. Thus, it is necessary to validate these models at low Reynolds numbers or develop approaches and models specifically for low Re situations. Surface roughness has a considerable impact on the heat transfer process [58,59] and heat transfer (especially convective heat transfer) is one of the significant mechanisms that control the ice accretion process [60]. Roughness also has a major influence on the fluid flow and droplet impingement module of the ice accretion modeling [61,62]. Therefore, the final ice shape is very sensitive to the evolution of local surface roughness at the start and during the ice accretion process and this demands efficient roughness models. Accurate experimental results are mandatory to enhance the existing numerical models and develop new models. The lack of proper experimental results for ice accretion at low Reynolds number still remains a gap in this area.

3. Effect of Environmental, Geometrical, and Material Conditions on Ice Accretion

By the beginning of the 21st century, more researchers started working on icing-related issues of UAVs. Most of them were concentrated on studying the sensitivity of nature and the shapes of accreted ice to environmental and geometric conditions. The nature of the ice forms depends primarily on free stream velocity (V_∞), atmospheric temperature (T_∞), Liquid Water Content (LWC), the droplet Median Volume Diameter (MVD), angle of attack (α), Reynolds number (Re), and the geometry of the structure (airfoil, chord, mean effective camber and material). In this section, an attempt is made to review the studies by various researchers to understand the influence of these parameters on the ice accretion behavior of UAVs at low Reynolds number values. The results presented in this section are mainly based on numerical studies using various ice accretion simulation codes.

3.1. Effect of Atmospheric Temperature (T_∞)

The effect of atmospheric temperature (T_∞) on ice accretion of a UAV was studied by Koenig et al. in 2001 [63] and Szilder in 2011 [25,64]. The nature of the ice changed from glaze to rime with a mixed ice behavior in between with a decrease in T_∞. In both these studies, the influence of T_∞ is studied independently by keeping the MVD and LWC value constant. However, the parameters are no longer independent when the studies are based on the FAR 25 Appendix C icing envelope. Such studies were done by Szilder in 2015 [65], 2017 [66], Krøgenes and Hann in 2017 [57,67], and Fajt in 2019 [68] on different airfoil geometries. The observations were qualitatively similar to Szilder's initial studies that the low temperatures favor rime ice formation and glaze formed at a temperature near the freezing point with mixed ice formed in between. For temperatures very close to the freezing point like $T_\infty = -2\ ^\circ\mathrm{C}$ the heat transfer process is not high enough to freeze all the droplets upon impingement, therefore a part of the impinging droplets runback along the airfoil surface leading to the glaze ice formation. Whereas at very low temperatures of $T_\infty = -10\ ^\circ\mathrm{C}$ and above, most droplets freeze upon impingement leading to rime ice formation. Additionally, it was observed that the rime ice formed at lower temperatures ($-30\ ^\circ\mathrm{C}$) is just a scaled-up version of the same at higher temperatures ($-10\ ^\circ\mathrm{C}$), this is due to the low value of the LWC at higher negative temperatures as defined in the FAR 25 Appendix C icing envelope. Fajt also pointed out that the ice mass increases with temperature.

3.2. Effect of LWC and MVD

The combined effect of LWC and MVD on ice accretion of UAV was studied by Koenig et al. [63] in 2002. The ice shape changes from smooth rime ice with no oblique protrusion or horns to glaze ice with two enormous horns when the LWC and MVD values increase. Additionally, a considerable rise in the amount of ice deposited is observed. In 2011, Szilder studied the influence of LWC independently on the ice accretion behavior by keeping the MVD or LWC and T_∞ constant [25,64]. For temperature greater than -8 °C, the ice shape changes from rime to mixed (glaze ice formed at the stagnation leading edge and rime ice formed in the downstream region) and then to glaze ice with water run back along the surface with an increase in LWC. Szilder [64] also pointed out that an increase in the size of the droplet tends to diminish the parametric space for rime but increases the space for the glaze. When the investigations are done based on FAR 25 Appendix C icing envelope [55,64–67], the ice accreted is a function of T_∞, MVD and LWC values. Smaller MVD values correspond to large LWC values and favored glaze ice formation. When the LWC is large, the latent heat that must be removed in order for the impinging droplets to completely freeze is also large, thus favoring glaze ice. However, T_∞ also plays an important role here as the potential to remove the latent heat increases at lower temperatures. Fajt [68] observed that when the LWC is less than 0.2 g/m^3, the ice formed is always streamline shaped (rime) irrespective of MVD and T_∞. When Li [69] studied the effect of LWC and MVD based on the FAR 25 icing envelope in 2020, it was observed that as the value of MVD increases, the size of the ice horns decreases because of the reduction in the LWC. With further increase in MVD, the presence of a horn has completely vanished, and ice accreted in a streamlined fashion, increasing the effective camber and enhancing the aerodynamic performance. From the analysis of droplet trajectories, Szilder inferred that the larger droplets have higher inertia and have a slower response to the spatial variations in the flow. It increases the collision efficiency and leads to a greater impingement extent. At temperatures close to freezing point, the heat transfer rate is not high enough to freeze all the water droplets leading to a glaze ice formation with water runback. Additionally, the smallest droplets result in the greatest local maximum ice thickness (especially at the leading edge) due to the large value of LWC as per the Appendix C icing envelope. Similar observations were also made by Avery [26]. However, a contradicting observation is made by Cistriani in 2007 [70] as a part of his studies on the design of Low *Re* airfoil for the Falco UAV. The formation of the worst ice shape at Continuous Maximum (CM) conditions with a low value of LWC compared to Intermittent Maximum (IM) conditions with higher LWC values is mentioned. Since this study was not dedicated to icing issues, much information regarding the software used and ice shapes formed at the remaining conditions is unavailable. Koenig [10] in 2003 pointed out that the clustering of the LWC value also has an effect on the ice accretion based on his icing tunnel test with constant and variable rate LWC.

3.3. Effect of Reynolds Number (Re)

The ice accretion behavior at high *Re* has been widely studied in the literature but a direct transformation of these results to low *Re* is not possible due to the problems discussed in Section 1. Therefore, Szilder in 2011 [64] studied the effect of *Re* on the ice accretion behavior by conducting numerical icing studies at two different *Re* of 5×10^6 and 5×10^4 [25,64]. The Reynolds number is varied by changing the values of V_∞ and C. The nature of the ice changes from rime to mixed and then to glaze with an increase in LWC for low *Re*. Whereas the nature of the ice remains glaze for all the values of LWC at high *Re* with only the extent of ice increasing with LWC. Further the thickness of the ice is considerably smaller when compared to the low Re number cases. The reduction in the thickness and decrease in the rate of icing can be attributed to the high values of aerodynamic heating at higher velocities. Low Reynolds favors the formation of rime ice which results in less aerodynamic penalties, but at the same time increases the relative ice thickness making the total ice mass high.

3.4. Effect of Free Stream Air Velocity (V_∞)

Bottyan et al. in 2013 [71,72] observed that the increase in true airspeed from 10 m/s to 130 m/s changes the ice behavior from less dangerous dry ice to more dangerous wet ice with horns at $T_\infty = -4.2$ °C. Further, an increase in the rate of icing with velocity is also observed. Ice thickness at the stagnation region decreases, and it completely vanishes at higher velocities leading to the formation of horns at an oblique angle with the surface. The horns also got thicker and thicker with velocity. The decrease in the leading-edge ice thickness can be because of the increase in the aerodynamic heating at higher velocities. In 2021, Hann et al. [55] concluded that the free stream velocity significantly affects the ice accretion behavior of the glaze and mixed ice more than rime ice. As the velocity increases, the streamwise thickness of glaze ice decreases, whereas the spanwise extension increases. At a very high velocity of 100 m/s, no ice was formed for the glaze icing conditions due to increased surface temperature beyond the freezing point because of aerodynamic heating. For mixed ice conditions, a large value of velocity is chosen by Krøgenes and Hann [57,67] to obtain artificial ice shapes with distinct horn shape formation. It is in line with the observation of Bottyan et al. [71] that an increase in the velocity leads to the formation of significant horns near the leading edge.

3.5. Effect of Angle of Attack (α)

In 2015, Szilder et al. compared the UAV ice accretion behavior at cruise conditions with $\alpha = 3^\circ$ to the same at landing flight conditions with $\alpha = 9^\circ$ [65]. During landing, the large value of angle of attack increases the vertical component of drop velocity than cruise conditions and the droplet impingement (and therefore the extent of ice formation) is more on the lower surface of the airfoil. For the ice shapes obtained for landing conditions, the stagnation region is shifted due to the large angle of attack, and a corresponding shift in the icing location is observed. A similar shift is observed during the icing tunnel studies of Williams on RG-15 airfoil [27].

3.6. Effect of Geometric Parameters

Various geometric parameters such as airfoil chord length, mean camber, thickness, aspect ratio, and leading-edge cylinder diameter can affect ice accretion by influencing flow behavior, droplet trajectories, and rate of heat transfer. Hann et al. in 2021 [55] studied the effect of change in chord length on the ice accretion behavior and observed that the extent of icing and its thickness increases with a decrease in chord length. In 2017, Szilder et al. performed ice accretion studies on various UAV airfoils [66] and concluded that the ice mass accumulated is small on a thinner airfoil. The ice thickness at the stagnation point is very similar, but differences in the ice extends are observed. This could be due to variations in the vertical component of drop velocity near an airfoil.

Most existing literature on numerical studies of UAV icing is limited to 2D airfoils. An ice accretion simulation on a 3D swept wing was performed by Szilder et al. in 2017 [66]. The ice mass increased towards the wing root section because of growing wing thickness near the root. The ice thickness decreases as we move along the leading edge from tip to root because of the decrease in convective heat transfer coefficient in that direction due to the reduction in velocity. Additionally, the extent of ice accretion is greater towards the root section due to the water runback caused by less efficient freezing of water and a large impingement mass. The changes in the ice accretion behavior along the spanwise direction were also observed due to the difference in local chord length and wing shape. Yirtici in 2020 [73] performed numerical icing simulations on a rectangular wing with NREL S826 airfoil at three different aspect ratios and it was observed that the loss in C_L/C_D decreases with the increase in wing aspect ratio.

3.7. Effect of Material Properties

In 2018, Li investigated the effect of thermal conductivity on ice accretion on the airframe surface [17]. The ice accretion process on aluminum (representing the manned

aircraft) and thermoplastic material (representing UAV) were investigated during the studies. Under the same operating conditions, the thermoplastic material with a lower thermal conductivity value causes a much slower dissipation of the released latent heat of fusion associated with the solidification of the supercooled water droplets impinging on the surface. Thus, resulting in water runback and the formation of more complex ice structures like rivulets when compared to the aluminum surface with higher thermal conductivity.

Discussion: The investigations revealed the influence of various environmental geometric and material properties on ice accretion. Reynolds number, free stream velocity, and chord length can significantly influence the ice accretion behavior. These parameters distinguish the operating conditions of manned aircraft from that of UAVs. Therefore, the ice accretion phenomenon on a UAV needs to be studied separately from that of manned aircraft. Siquig [16] reported the most vulnerable icing conditions as T_∞ between 0 to -10 °C, LWC more than 0.1 g/m^3, and droplet diameter between 30 and 400 microns. Rime ice formation is favored at low temperatures, whereas glaze is formed at a temperature near the freezing point with mixed ice formed in between. All the other factors discussed above can influence the icing extend, thickness, horns, ice lobes, and feather-like structures. Szilder [65] concluded that the extent of ice formation increases with drop size, but LWC mostly governs ice thickness. Fajt [68] observed the highest ice mass at MVD of 20 µm and $T_\infty = -2$ °C even though the LWC value at MVD of 20 µm is 20% less than the same at MVD of 15 µm, this can be because of the larger droplet size. Thus, the nature and shape of ice formed can be considered as a function of the complex interplay of various environmental and geometric parameters. Most studies are concentrated on the temperatures of $T_\infty = -2$ °C, -5 °C and -10 °C with the corresponding LWC and MVD values proposed by Appendix C of FAR 25. It is observed from various studies that glaze ice conditions can lead to more complex ice shapes, with a special case of mixed icing conditions at $T_\infty \geq -4$ °C. Thus, the ice accretion studies need to be refined to more temperature conditions between -2 °C and -10 °C. Additionally, the detrimental effect of Supercooled Large Droplets (SLD) is discussed in the literature, but the same is not studied from the scope of low Reynolds number problems or UAVs. Since ice accretion is a dynamic process and is highly sensitive to atmospheric and geometric conditions, the nature and shape of the ice formed can differ from the expectations. Therefore, a correlation between various geometric and environmental conditions and the ice formed cannot be easily made. However, such attempts can be made from a research point of view so that future researchers can correlate their predictions with these benchmarks and the variations can be reported.

4. Aerodynamic Performance Penalties

Aerodynamic performance penalties can be considered as a significant consequence of ice accretion on airfoil structures. So, it is essential to understand how icing affects the aerodynamic performance of an airfoil. To study iced airfoil aerodynamic penalties, one can use an icing wind tunnel like the NASA IRT, where the aerodynamic forces are recorded simultaneously with the ice accretion process. This can be considered as the precise method of measuring the aerodynamic forces and moments of the iced airfoil as the process is fully transient. To the author's knowledge, no such experiments have been reported for a fixed-wing UAV in the open literature to date. Another option is to 3D print the iced profile obtained from an icing tunnel test or numerical simulation and attach it to the airfoil's leading edge. It is then tested in a wind tunnel to determine the aerodynamic forces and moments. Most researchers employ this approach because conventional wind tunnels are more readily available than icing wind tunnels. However, the accuracy of the measurements is compromised in this method because the ice shapes and aerodynamic forces are measured only for a particular instant of time and are no longer transient. In addition, the ice shape generated for a specific angle of attack (at which the numerical simulation or icing tunnel experiment is carried out) is used to study aerodynamic performance as a function of the angle of attack. In a way, this can lead to

misleading results as the shape, location, and nature of the ice accreted changes with the angle of attack and affects aerodynamic forces and moments. Both approaches can also be used in numerical studies to predict the aerodynamic coefficients of an iced airfoil.

Cistriani et al. in 2007 [70] studied the aerodynamic performance of an iced UAV airfoil in the wind tunnel. Icing reduced the maximum lift by 30% compared to the clean airfoil. Szilder et al. performed the aerodynamic simulation of iced UAV airfoils SD7037 [65], HQ309, and SD7032 [66] with the ice shapes obtained from MORPHICE simulations. The turbulence model employed is the $\gamma - Re_{\theta t}$ transition model [74]. In glaze ice conditions at -2 °C the SD7037 airfoil lost 16% lift, tripled drag (300%) and stalled prematurely at 9° (clean airfoil stalls at 11°) along with a 12% decrease in pitching moment. The aerodynamic penalties for rime ice are relatively smaller as it covers only a smaller portion of the airfoil. It is worth noting that for large values of angle of attack, the aerodynamic performance improved for the glaze ice more than rime ice. The author attributes this to the increase in the effective camber due to the drooped leading edge, which delays the flow separation. Overall, HQ309 with less thickness has better aerodynamic performance than SD707 at a low value of α, and is reversed at higher α values. SD7032 revealed the best aerodynamic performance at rime ice condition. The observations were based on numerical results and no experimental validation is performed at low Reynolds number.

Hann et al. conducted wind tunnel studies on iced NREL S826 airfoil with the ice shape obtained from the LEWICE simulations [67] and the icing tunnel experiments [57]. Surface roughness effects were superimposed on the models using half-spheres arranged in a staggered pattern. The diameter of the sphere is the equivalent sand grain roughness (k_s) calculated using an empirical relation proposed by Shin et al. [31]. Former studies show severe performance penalties for the mixed ice with 30% reduction in lift and 340% increase in drag due to flow separation induced by the presence of horn structures. In contrast, the icing tunnel predicts more complex ice shapes for glaze conditions, and no prominent horns were observed for mixed ice conditions. Therefore, glaze ice had the largest aerodynamic penalties. Low Reynolds number indicates severe performance penalties, as does the increased surface roughness, especially for rime ice. In 2018, Hann [52] compared the aerodynamic performance of the ice shapes predicted by FENSAP ICE and LEWICE codes using the fluid flow solver FENSAP employing the SA turbulence model. The significant difference in the ice shape predicted by both codes was also reflected in the aerodynamic behavior. Overall, mixed ice showed severe performance degradation followed by glaze and rime. Further, numerical simulations were done with a forcibly tripped boundary layer and compared with the fully turbulent simulations. The tripped cases showed slightly higher performance penalties comparatively [57]. Severe aerodynamic penalties of RG-15 airfoil at glaze ice conditions with an increase in drag coefficient up to 160% were also reported by Fajt [68] based on his numerical studies using FENSAP and by Oswald [75] based on his experiments at wind tunnel facility. Fajt [68] also presented an index visualization of the aerodynamic coefficients to understand the intensity of performance degradation for different icing conditions, as shown in Figure 4. In 2021, Hann [55] reported that the increase in flow velocity has a detrimental effect on the aerodynamic performance of an RG15 airfoil, whereas an increase in chord length is favorable.

The numerical and experimental research forecast aerodynamic coefficients differently [57]. Viscous boundary layer effects overwhelm the inertia effects at low Reynolds numbers, favoring laminar flow. Existing turbulence models presume fully turbulent flows and hence cannot accurately resolve these issues. Flow transition from laminar to turbulent is another challenge; the initial laminar flow is so sensitive that even a mild pressure gradient can separate the flow. The separated flow re-attaches under certain flow conditions and forms a Laminar Separation Bubble (LSB) while transitioning from laminar to a turbulent state. LSB is a function of airfoil geometry and flow velocity and can be observed in the Reynolds number regime of 5×10^4 to 3×10^6 [76]. The flow separation induced by ice formation on the airfoil's leading edge is called an Ice Induced Separation Bubble (ISB) [77]. The ISB formed immediately downstream of the accreted ice at the

leading edge, increasing its size with α. In contrast, an LSB formed downstream from the leading edge and moved upstream with increasing α. The formation of ISB or LSB changes the behavior of the boundary layer from laminar before separation to turbulent after reattachment. Additionally, the size of the LSB is contracted with the increase in *Re* [78], leading to complex flow behavior at low Reynolds numbers.

Oo et al. performed studies on clean and iced RG-15 airfoil to understand the behavior of LSB and ISB (Figure 5). The ice shapes were adopted from the icing tunnel studies of Williams [27]. In 2018 [79], unsteady numerical simulations were done by employing the Scale-Adaptive Simulation-Shear-Stress Transport (SAS-SST) model for turbulence [80]. LSB is not observed, and the flow is fully turbulent for the angle of attack considered. He extended the studies by performing transient Large Eddy Simulations (LES) at a different angle of attack (0°, 3° and 6°) in the successive years [81,82]. LSB is not observed on a clean airfoil at $\alpha = 0°$, but separation near the trailing edge is observed. With an increase in value of α, LSB is formed downstream of leading edge, and it moves upstream with further increase of α. ISBs are observed for the iced airfoil and the extend of separation bubble increased from 10 to 13% of the chord with increase in angle of attack, but the origin of separation remains the same. High frequency oscillations were observed in the transitional regions of ISB and LSB [83]. The frequency of these oscillations can sometimes be higher than the vortex shedding frequency of an airfoil [84]. The author also concluded that the characteristics of ISB and LSB are pretty similar, which agrees with the previous observation made by Bragg [85]. Oo [83] further extended the studies to a lower Reynolds number of 5×10^4. One of the key observations is that the flow reattachment is delayed for low Reynolds numbers and the extent of separation increases. The formation of a secondary separation bubble for $\alpha = 2°$ and 3° at a low Reynolds number is also observed. Similar observations on the behavior of LSB on RG-15 airfoil are also made by Oswald [75,86]. In contrary to all previous observations on aerodynamic behavior, Oo observed an increase in the lift coefficient from 0.11 to 0.22 and a decrease in drag for iced airfoils compared to clean airfoil (RG-15). The author suggested that the lift increment can be due to the boundary layer tripping, and the drag reduction can be due to the larger laminar separation bubble on clean airfoil relative to the ice induced separation bubble.

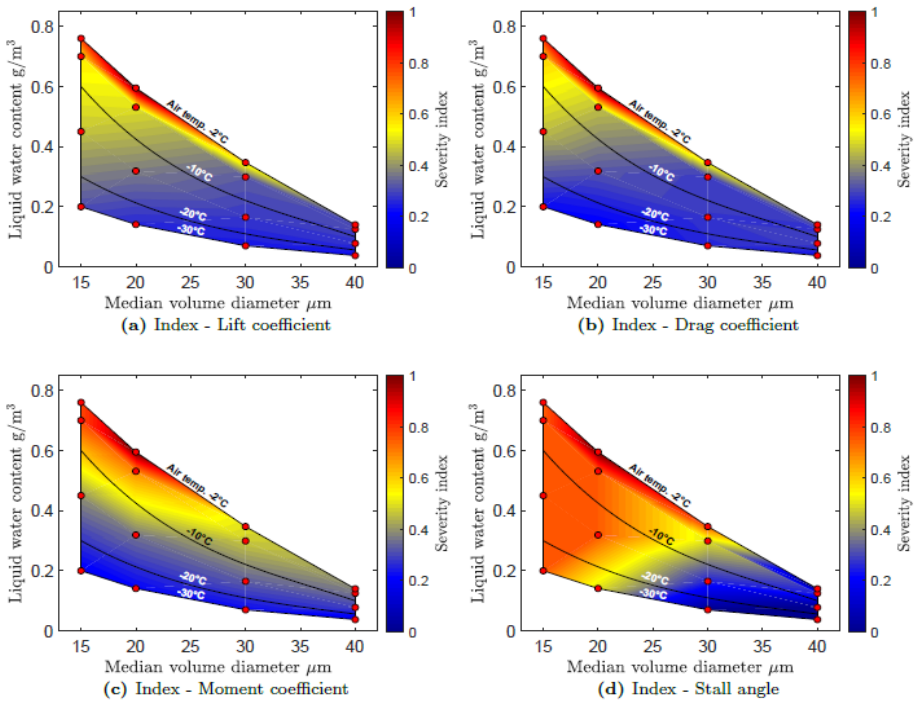

Figure 4. Index visualization for the aerodynamic performance of RG-15 airfoil [68].

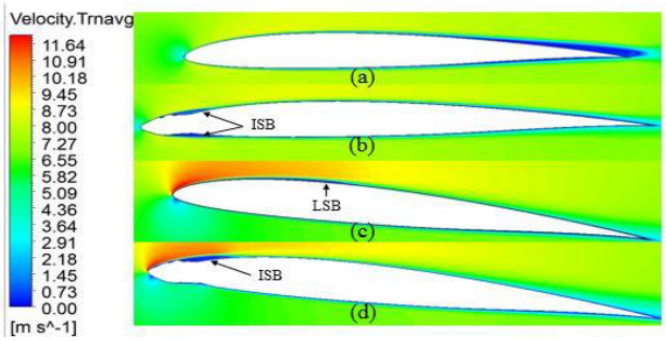

Figure 5. Formation of Laminar Separation Bubble (LSB) and Induced Separation Bubble (ISB): (**a**) 0° clean, (**b**) 0° iced, (**c**) 6° clean, (**d**) 6° iced [81].

A transitional three-equation turbulence model with a separated shear layer fix called the SPF $k - v^2 - \omega$ model [87] was used by Li in 2020 [69] to investigate the aerodynamic performance of an iced NREL S826 airfoil. It is observed that the pre-stall and near-stall characteristics predicted by the turbulence model match well with the experimental results compared to SST and SA turbulence models, which usually fail in the region close to the stall. The maximum loss in lift coefficient is 24.3% and the stall angle decreases by 6 degrees. One of the major attractions of this paper is the optimization of the airfoil design under icing conditions. The optimized airfoil design improves the lift coefficient by 18% by modifying the ice shape.

Discussion: It can be concluded from the reviewed work that icing can lead to severe aerodynamic penalties like loss of lift, an increase of drag, and premature stalling. A maximum reduction in the lift of up to 35% and an increase in drag of up to 340% is observed in UAVs due to ice accretion. Premature stalling also occurs at an angle of attack as low as 7°. The reduction in the maximum lift value affects the stability of the UAV and the increase in the drag coefficient leads to more power consumption. This can potentially limit the range and endurance of the UAV and thus affect the successful completion of its mission. Koenig [63] pointed out that glaze ice has a more significant impact on aerodynamic characteristics due to the greater surface roughness and larger extend. Further, glaze ice can lead to the formation of horns at an oblique angle with the surface, which in turn can lead to flow separation. The magnitude of the aerodynamic penalties depends on the shape, location, and extend of the ice accreted. The accumulated ice also adds weight to the structure of the UAV, which also has an indirect effect on its performance. The magnitude of the performance degradation is a function of ice shape, location, and extent. Fajt [68] highlights that one of the important uncertainties in the icing simulation is the assumption of fully turbulent flow. This can be valid for high values of angle of attack, due to the earlier flow separation but, for a small angle of attack, the flow can still be laminar at the leading edge. Thus, the assumption of fully turbulent flow induces artificial viscosity affects the delay of any possible flow separation. This can lead to overprediction of the lift coefficient and stall angle while underpredicting the drag coefficient. Additionally, the turbulent flow may increase the evaporation rate and thus reduce the liquid content leading to the wrong prediction of ice shapes as emphasized by Hann [88]. Thus, proper transition turbulence models must be implemented to model the laminar-turbulent transition phenomenon. Most studies are limited to the use of the SA and K-ω SST turbulence model, but they failed to predict the stall angle and maximum lift coefficient of the iced airfoil. Most existing studies used the profile of ice accreted at an 0° angle of attack to study aerodynamic performance as a function of the angle of attack. However, the position of ice changes with the angle of attack and leads to a considerable difference in the value of aerodynamic coefficients. Therefore, representative ice shapes at different angles of attack must be used to obtain more reliable aerodynamic coefficients. A database for various studies related to icing on fixed wing UAVs is given in Table 1.

Table 1. Database of existing studies on ice accretion on Unmanned Aerial Vehicle (UAV).

Reference	Year	$Re \times 10^5$	Airfoil	C (m)	Aerodynamic Data	Comments
Siquig [16]	1990	-	-	-	×	The impact of icing on two different UAVs is compared.
Koenig [63]	2000	-	UAV airfoil	-	×	Influence of T_∞, LWC, and MVD on ice accretion.
Koenig [10]	2003	-	NACA 0012	-	×	Influence of LWC clustering on ice accretion.
Avery [26]	2003	-	-	-	×	Influence of T_∞ and LWC on ice accretion.
Cistriani [70]	2007	10	flap slotted airfoil	0.6	✓	Ice accretion at CM and IM conditions.
Szilder [64]	2011	0.5, 1, 5, 1, 50	NACA 0012	0.0625 to 0.625	×	Influence of Re, T_∞, LWC and MVD on ice accretion.
Szilder [25]	2012					
Bottyan [71]	2013	4	Roncz Low Drag airfoil	0.3	×	Influence of V_∞ on ice accretion.
		40	NASA NLF 1015	1.6		
Szilder [65]	2015	9	SD7037	0.47	✓	Influence of T_∞, α, LWC, and MVD on ice accretion.
Szilder [66]	2017	9	HQ309, SD7032SD7037	0.47	✓	Effect of airfoil geometry on ice accretion.
Williams [27]	2017	2	RG15	0.21	✓	Icing tunnel experiments for 4 different cases.
Hann [89]	2017	15	NREL S826	0.3	✓	Aerodynamic performance studies based on flight simulation.
Hann [52]	2018	4	NREL S826	0.45	✓	Comparison of LEWICE and FENSAP-ICE.
0o [79]	2018	2	RG-15	0.21	✓	Flow separation behavior is studied using the SAS-SST turbulence model.
0o [81]	2018	1	RG-15	0.21	×	Flow separation behavior is studied using LES.
Fajt [68]	2019	8.6–10	RG-15	0.45	✓	Influence of T_∞, LWC, and MVD on ice accretion.
Hann [54]	2019	8.7	NREL S826, RG-15	0.45	×	Icing Tunnel studies, Two new ice shape acquisition techniques are discussed.
Hann [57]	2020	4	NREL S826	0.45	✓	Aerodynamic data is generated for three different Re of 2×10^5, 4×10^5, 6×10^5.
Oo [82]	2020	1.07	RG-15	0.21	×	Flow separation behavior is studied using LES.
Oo [83]	2020	0.5, 1	RG-15	0.21	×	Flow separation behavior is studied using LES.
Yirtici [73]	2020	4	NREL S826	0.45	✓	Influence of aspect ratio on ice accretion.
Oswald [75,86]	2021	8.7	RG-15	0.45	✓	Aerodynamic data is generated for three different Re of 2×10^5, 4×10^5, 7.5×10^5.
Hann [55]	2021	8.7	RG-15	0.45	✓	Effect of velocity and chord length on ice accretion.
Li [69]	2021	20	NREL S826	0.45	✓	A three-equation turbulence model is used, Design optimization of airfoils.

5. Effect of Icing on the Structural Integrity of UAVs

Ice accretion is a dynamic process, and the distribution of ice on the surface of a UAV wing or propeller blade is not uniform. Most ice accreted on the stagnation regions like the leading edge of wings or propellers, with the amount of ice accretion increasing from root

to tip of the propeller blade. Further, the melting and ice shedding effects also contribute to uneven mass distribution. This mass imbalance can cause excessive vibrations. The ice accretion on the leading edge of the airfoil also shifts the center of gravity towards the elastic axis (increasing the critical flutter speed), increases the mass and inertia properties, increases the effective chord length, increases the aerodynamic drag and pitching moment loads, and decreases the lift [90]. These changes in the aerodynamic and structural behavior due to ice accretion can change the wing's modal properties (natural frequencies and damping ratio). They may lead to resonance and excess vibrations, affecting the aeroelastic behavior [91] and fatigue life of the structure [92]. These fatigue loads considerably reduce the lifetime of the UAV structure. Lighter systems like UAVs are more susceptible to aeroelastic instabilities like flutter. Studies related to the understanding of the effect of ice accretion on UAVs' structural behavior are not developed and need to be addressed to avoid potential structural damages. Similar studies were done on wind turbine applications and other structures. A detailed review of such works is not intended here, but a few of them are addressed here as a motivation for similar studies on UAVs. Etemaddar [92] pointed out that "*The aerodynamic properties are affected from the early stage of icing due to change in roughness and geometry of the leading edge of the blade, whereas the change in structural properties needs longer time and more ice accretion*". Additionally, he pointed out that the effect of icing on fatigue life is negligible due to the short duration of operation under icing conditions compared to the total lifetime.

In 2016, Gantasala et al. [91] studied the influence of ice accretion on the modal behavior of wind turbines. The natural frequency and damping factor of the blade decrease with ice accumulation. The ice mass distributed along the blade length determines the rate of reduction in frequencies. The damping factor is a function of aerodynamic coefficients; therefore, it depends mainly on the ice shape. It is also observed that the damping factor has a more considerable reduction due to icing than the natural frequencies. The variation of natural frequencies of the iced blade with wind velocities is negligible. Reducing the damping factor to even negative values is observed at higher velocities, leading to unstable vibrations. In 2017 [90], he conducted studies to understand the effect of aerodynamic and structural responses on flutter instability. As the ice mass increases, the center of gravity moves towards the elastic axis, and the flutter wind velocity increases. The flutter velocities also tend to decrease when considering the chord length increase. This can be due to increased pitching moment loads with the chord length. When aerodynamic behavior is also considered, the flutter velocity increases for ice shapes with lower aerodynamic loads and vice versa. Thus, the changes in the aerodynamic performance due to icing can be considered a critical parameter that alters the flutter instability. Thus, the accumulation of ice mass on the wing reduces its natural frequency and damping factor, decreasing the flutter wind velocity, and increasing the risk of aeroelastic instability. If resonance occurs, it can lead to excess vibration leading to failure and near-resonant vibrations can reduce the fatigue life of the wings.

6. Ice Detection and Ice Mitigation Techniques

Anti-icing and de-icing systems are the two types of Ice Protection Systems (IPS). The anti-icing mode heats the structure surface continually to prevent ice formation and can be done in two ways: *fully evaporative or running wet*. There can be no water run back in the first mode because the heat supplied entirely evaporates the droplet at the impingement location. However, it requires considerable heat flux and results in high surface temperatures. In the latter option, the heat is only used to keep the water from freezing. This mode requires less heat flux and lower surface temperature, but the surface must be heated extensively to prevent droplet freezing during water runback. In de-icing, ice is allowed to accumulate on the surface, and heat is used to melt it. The ice-surface interface can be melted or shed by aerodynamic forces. Dei-icing uses less power, but the accumulated ice might cause drag and structural damage during ice shedding. The problem of ice accretion on manned aircraft is extensively investigated, and suitable ice mitigation

techniques are developed [19,93]. Traditional aircraft anti-icing methods use heat from engine bleed air, electro-thermal systems, or freezing point depressant chemicals to prevent ice buildup. Electromechanical systems like pneumatic de-icing boots, electro-expulsive systems, and electro-impulsive systems are typically used as de-icing systems. These systems are sophisticated, power-hungry, and require regular maintenance, limiting their use in smaller aircraft or UAVs.

Proper ice detection techniques need to be developed for the successful operation of an IPS. A brief overview of such systems designed for UAVs is done here before going to the review of an IPS. Botura [94] developed an Ice/No-Ice Sensor System (INISS) based on impedance measurement technique for in-flight ice detection on UAVs in 2003. The sensors are capable of detecting even thin coatings of ice. Cristofarao et al. (2015) proposed a Multiple Model Adaptive Estimation (MMAE)-based ice detection system for UAVs [95]. Unknown Input Observer (UIO) methods detect and estimate ice using changes in equilibrium caused by ice accumulation. A UIO-based ice detection method for UAVs with linearized longitudinal motion is proposed by Cristofaro et al. in 2015 [96]. This method is extended to the longitudinal nonlinear aircraft dynamics using Linear Parameter Varying (LPV) methods by Rotondo in 2015 [97]. Seron in 2015 [98] coupled the UIO and MMAE methods to develop an ice detection system with prespecified accuracy. An icing detection method based on the diagnosis of lift and drag changes on a UAV wing was proposed by Sørensen et al. in 2015 [99] and was modified by Wenz et al. in 2016 [100]. Rotondo developed an icing detection system that provides information about the icing location in 2017 [101]. The author published an extension of this work in 2019 [102]. A Fault Detection and Isolation (FDI) framework that uses model-based estimators of the various faults, implemented with multiple Kalman and Bayes filters, was proposed by Haaland et al. in 2021 [103].

Electromechanical de-icing systems shed the ice by applying impulse force on the wing surface with the help of some actuators. In 1988, Leonard Haslim invented the Electro Expulsive Separation System (EESS) consisting of two conductors embedded in a flexible material glued to the wing's leading edge. The magnetic fields of the conductors repel each other when current flows through them and provide enough impact to melt the ice [104]. Bhakta proposed a magnetostrictive de-icing method for UAVs in 2005 [105]. When the magnetostrictive materials are magnetized, they exhibit a change in length and create an impulse action. The ability of piezoelectric crystals to strain under an applied electric field is called the piezoelectric effect. The waves, generated through piezoelectric patches bonded onto the inner surface of the wing skin, cause a shear action at the ice/skin interface [106]. The magnitude of this shear action is amplified at specific excitation frequencies (Lamb waves), corresponding to wave lengths commensurable with the skin thickness. In 2014, Ameduri et al. [107] investigated the use of lamb waves as dei-icing systems for UAVs. The ultrasonic sound waves propagating at low frequency into a material can cause vibrations and debonding [108]. Shape Memory Alloy (SMA) on heating can change shape and create force through a martensitic phase shift [109].

Carbon Nano Tubes (CNT) have excellent electrical and thermal conductivity, making them ideal for de-icing UAVs using the Joule heating property of conductors [110–115]. Buschhorn et al. [110] in 2013 developed a CNT-based IPS, which can prevent icing with a power supply of only 1 kw/m^2 during less harsh icing conditions. In 2015, Sørensen et al. developed an electrically conductive paint based on graphene and carbon black nanoparticles that heat up when electricity passes through it [116]. A disadvantage of this system is the power consumption and increase in the weight of the UAV because of the coating, battery, and other components. Thermodynamic analysis [117] and flight testing [118] of the IPS are performed in successive years. The icing conditions at the high airspeed and low ambient temperature necessitate significant power consumption. In 2020, Idris et al. [115] used extrusion printing to fabricate electrical contacts on carbon fibers. The carbon fiber composites are then integrated into UAV wings to create a self-heating de-icing mechanism.

The carbon-based materials can shield the radio frequency signals, so an RF transmitting heat was proposed by Hwang et al. in 2020 [119].

Hann et al. [88] evaluated LEWICE with FENSAP ICE for simulating and estimating anti-icing loads in 2019. A sudden increase in the heat flux is observed at the transition region as the rate of convective heat transfer increases due to higher turbulence. The studies reveal the necessity of proper transition modeling for the icing studies at low Reynolds numbers. Hann [120] then tested Sørensen's IPS mounted on a wing with RG-15 airfoil for ice detection, anti-icing, and completely autonomous capabilities. The stagnation point at the leading edge has the highest power requirements. The author also concluded that the average heat flux numbers might not be a fair estimate of overall necessary heat loads, but the peak values around the leading edge are more significant. Hann et al. [120] tested the anti-icing, de-icing, and Parting Strip (PS) approach for ice mitigation on the same IPS in 2021. In the PS method, the stagnation zone at the leading edge is continuously heated to avoid ice formation, separating the ice on the upper and lower part of the airfoil. The ice split increases the aerodynamic force on the ice and allows for better shedding, as shown in Figure 6. The parting strip model requires substantially less shedding time and heat flux than conventional techniques. Thus, the author considers the parting strip mode as the most energy-efficient ice mitigation mode.

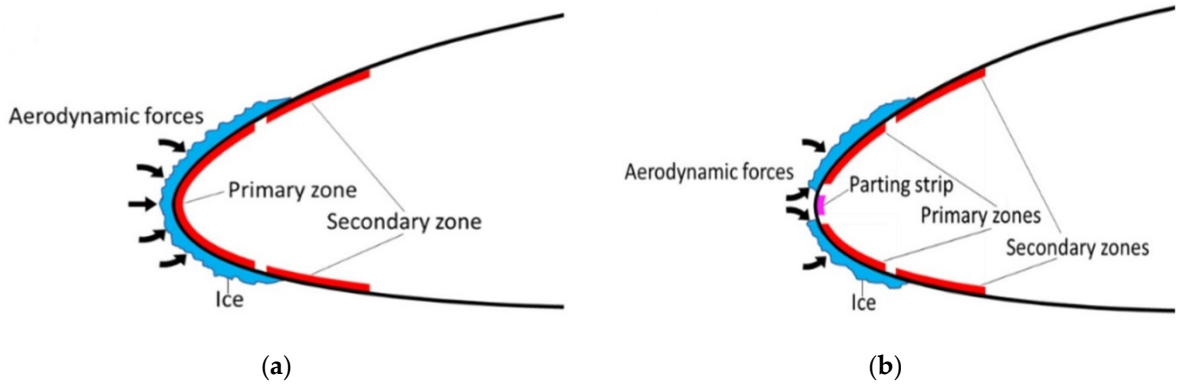

(**a**) (**b**)

Figure 6. Conventional (**a**) and Parting Strip (**b**) de-icing methods [120].

Superhydrophobic coatings can reduce the surface free energy and can generate hierarchical micro/nano-structured roughness. This can reduce the ice adhesion strength on the surface and thus prevent ice accumulation. Numerous studies related to different superhydrophobic coatings and the applicability of the same as an aircraft anti-icing material are done by Bhushan et al. [121–124] and Farzaneh et al. [23,125–129]. Ice accretion behavior of three different aluminum surfaces (hydrophilic, hydrophobic, and superhydrophobic) were compared by Wang in 2010 [130]. The research focuses on transmission line anti-icing; however, the findings can also be used for UAV ice mitigation. Initially, just a few portions of the superhydrophobic sample were coated with water droplets, whereas the hydrophobic was partially and the hydrophilic was entirely covered. Water droplets turned into the ice with increasing spraying time; however, no new ice crystals developed on superhydrophobic surfaces. Ice covered more of the hydrophobic surface and the whole of the hydrophilic surface with time. Thus, super hydrophobicity reduces surface wettability by increasing the average water contact angle to over 150°. The same for hydrophobic surfaces of more than 90° and for hydrophilic surfaces, it is less than 70°. Piscitelli [131] in 2020 proposed a superhydrophobic coating for small aircraft that can reduce the surface free energy by 99% with respect to the reference considered in the study. Additionally, the proposed coating was effective at temperatures as low as −27 °C.

Discussion: The following are the primary requirements for an efficient IPS: (1) lightweight, (2) low power consumption, (3) low maintenance and cost, and (4) reliable operation and short response time. (5) Minimal/no change in aerodynamic design. The main disadvantage of electromechanical and electrical heating systems is their weight. Continuous use

of electromechanical systems can cause structural damage, while electric heating requires more power, and superhydrophobic coatings degrade over time. As a result, an optimal ice protection system for UAVs that meets all requirements has yet to be developed.

7. Conclusions

The existing scientific knowledge about the ice accretion phenomenon on fixed-wing UAVs has been reviewed and the significant limitations in the current understanding of the same are identified. Icing tunnel experiments and numerical icing simulations are the most prominent methods used to study ice accretion. Icing tunnel experiments have the limitation of being unable to precisely generate the icing conditions found in nature, whereas numerical codes are lagging due to a lack of proper validation data. The capability of existing numerical icing codes in predicting the ice accretion for glaze ice conditions is limited due to the complex physics involved in its formation. Therefore, improved understanding and modeling of such physics are required. The shape, size, and nature of the ice formed are governed by the complex interplay of various environmental, geometrical, and material properties. The accretion of ice on the surface of an airfoil can deteriorate the aerodynamic shape of the airfoil as well as alter the surface characteristics like roughness, mean camber, and effective chord length. The variation of these parameters can alter the aerodynamic behavior by inducing flow transition (laminar to turbulent), flow separation, and it can also affect the distribution of pressure and shear force on the surface of the airfoil. Icing causes severe aerodynamic penalties like a decrease in the lift, increase in drag, and premature stalling. Therefore, the development of low-cost, lightweight, and energy-efficient ice mitigation systems is necessary to ensure the all-weather operation of UAVs.

Author Contributions: Conceptualization, M.M. and M.S.V.; methodology, M.M.; investigation, M.M.; data curation, M.M.; writing—original draft preparation, M.M.; writing—review and editing, M.M.; supervision, M.S.V. All authors have read and agreed to the published version of the manuscript.

Funding: The work reported in this paper is supported by the UiT- The Arctic University of Norway (Project no-7400-72104) & nICE project of UiT & Research Council of Norway (Project no-324156).

Institutional Review Board Statement: Not applicable.

Informed Consent Statement: Not applicable.

Data Availability Statement: The data presented in this study are available on request from the corresponding author.

Conflicts of Interest: The authors declare no conflict of interest.

References

1. Singhal, G.; Bansod, B.S.; Mathew, L. Unmanned Aerial Vehicle Classification, Applications and Challenges: A Review. *Preprints* **2018**, 2018110601. [CrossRef]
2. Gupta, S.; Ghonge, M.; Jawandhiya, P. Review of Unmanned Aircraft System (UAS). *Int. J. Adv. Res. Comput. Eng. Technol.* **2013**, *2*, 1646–1657. [CrossRef]
3. Alvarado, E. Drone Application Report 2021. 2021. Available online: https://droneii.com/237-ways-drone-applications-revolutionize-business (accessed on 15 January 2022).
4. Weatherington, D.; Deputy, U. *Unmanned Aircraft Systems Roadmap, 2005–2030*; U.S. Department of Defense: Washington, DC, USA, 2005.
5. Curry, J.; Maslanik, J.; Holland, G.; Pinto, J. Applications of Aerosondes in the Arctic. *Bull. Am. Meteorol. Soc.-Bull. Am. Meteorol. Soc.* **2004**, *85*, 1855–1861. [CrossRef]
6. Clark, D.G.; Ford, J.D.; Tabish, T. What Role Can Unmanned Aerial Vehicles Play in Emergency Response in the Arctic: A Case Study from Canada. *PLoS ONE* **2018**, *13*, e0205299. [CrossRef] [PubMed]
7. CAA. CAP 1036: Global Fatal Accident Review 2002 to 2011. In *Civil Aviation Authority 1036*; CAA: Los Angeles, CA, USA, 2013; pp. 1–134.
8. Haulman, D.L. *US Unmanned Aerical Vehicles in Combat 1991–2003*; Air Force Historical Research Agency: Montgomery, AL, USA, 2003.

9. Peck, L.; Ryerson, C.C. *Army Aircraft Icing*; Technical Report ERDC/CRREL TR-02-13; US Army Corps of Engineers: Washington, DC, USA, 2002.
10. Koenig, G.; Ryerson, C.; Larsson, J.; Reehorst, A. Effect of Variable LWC on Ice Shape in the NASA-GRC IRT. In Proceedings of the 41st Aerospace Sciences Meeting and Exhibit, Reno, NV, USA, 6–9 January 2003.
11. Li, N.; Liu, X.; Yu, B.; Li, L.; Xu, J.; Tan, Q. Study on the environmental adaptability of lithium-ion battery powered UAV under extreme temperature conditions. *Energy* **2021**, *219*, 119481. [CrossRef]
12. Wang, B.H.; Wang, D.B.; Ali, Z.A.; Ting Ting, B.; Wang, H. An overview of various kinds of wind effects on unmanned aerial vehicle. *Meas. Control* **2019**, *52*, 731–739. [CrossRef]
13. How Is an UAV Affected by In-Flight Icing and Can We Simulate It Accurately? Available online: https://uavicinglab.com/2021/05/28/how-is-an-uav-affected-by-in-flight-icing-and-can-we-simulate-it-accurately/ (accessed on 15 January 2022).
14. Avery, A.S. *Ice Accretion on Small Unmanned Aircraft*; Oklahoma State University: Stillwater, OK, USA, 2019.
15. Hacker, P.T.; Dorsch, R.G. *A Summary of Meteorological Conditions Associated with Aircraft Icing and a Proposed Method of Selecting Design Criterions for Ice-Protection Equipment*; National Advisory Committee for Aeronautics: Washington, DC, USA, 1951.
16. Siquig, R.A. *Impact of Icing on Unmanned Aerial Vehicle (UAV) Operations*; Naval Environmental Prediction Research Facility: Monterey, CA, USA, 1990.
17. Li, L.; Liu, Y.; Zhang, Z.; Hu, H. Effects of thermal conductivity of airframe substrate on the dynamic ice accretion process pertinent to UAS inflight icing phenomena. *Int. J. Heat Mass Transf.* **2019**, *131*, 1184–1195. [CrossRef]
18. Lynch, F.; Khodadoust, A. Effects of ice accretions on aircraft aerodynamics. *Prog. Aerosp. Sci.* **2001**, *37*, 669–767. [CrossRef]
19. Bragg, M.B.; Broeren, A.P.; Blumenthal, L.A. Iced-airfoil aerodynamics. *Prog. Aerosp. Sci.* **2005**, *41*, 323–362. [CrossRef]
20. Makkonen, L.E. *Ice and Construction*, 1st ed.; CRC Press: Boca Raton, FL, USA, 1994.
21. Makkonen, L. Modeling of Ice Accretion on Wires. *J. Appl. Meteorol. Climatol.* **1984**, *23*, 929–939. [CrossRef]
22. Makkonen, L.; Laakso, T.; Marjaniemi, M.; Finstad, K. Modelling and Prevention of Ice Accretion on Wind Turbines. *Wind. Eng.* **2001**, *25*, 3–21. [CrossRef]
23. Farzaneh, M. *Atmospheric Icing of Power Networks*; Springer: Dordrecht, The Netherlands, 2008.
24. Finstad, K.J. *Numerical and Experimental Studies of Rime Ice Accretion on Cylinders and Airfoils*; University of Alberta: Edmonton, AB, Canada, 1986.
25. Szilder, K.; McIlwain, S. In-flight icing of UAVs—The influence of flight speed coupled with chord size. *Can. Aeronaut. Space J.* **2012**, *58*, 83–94. [CrossRef]
26. Avery, A.S.; Jacob, J.D. Evaluation of Low Altitude Icing Conditions for Small Unmanned Aircraft. In Proceedings of the 9th AIAA Atmospheric and Space Environments Conference, Denver, CO, USA, 5–9 June 2017; p. 3929.
27. Williams, N.B.A.; Brian, G.; Ol, M. The effect of icing on small unmanned aircraft low Reynolds number airfoils. In Proceedings of the 17th Australian International Aerospace Congress (AIAC), Melbourne, Australia, 26–28 February 2017.
28. Matiychyk, L.; Suvorova, N.; Tereshchenko, D.; Plakhotniuk, I.; Trachuk, K.; Komarova, K. Influence of Icing on Aircraft Performance of Unmanned Aerial Vehicle M-10-2 "Oko". *Proc. Natl. Aviat. Univ.* **2017**, *4*, 52–59. [CrossRef]
29. Siddique, M.A. An Experimental Study on the Effects of Adverse Weathers on the Flight Performance of an Unmanned-Aerial-System (UAS). Ph.D. Thesis, Iowa State University, Ames, Iowa, 2021. [CrossRef]
30. Gray, V.H. *Aerodynamic Effects Caused by Icing of an Unswept NACA 65A004 Airfoil*; National Advisory Commitee for Aeronautics, Lewis Flight Propulsion Laboratory: Cleveland, OH, USA, 1958.
31. Shin, J.; Bond, T.H. Experimental and computational ice shapes and resulting drag increase for a NACA 0012 airfoil. In Proceedings of the Fifth Symposium on Numerical and Physical Aspects of Aerodynamic Flows, Long Beach, CA, USA, 13–15 January 1992.
32. Shin, J.; BOND, T. Results of an icing test on a NACA 0012 airfoil in the NASA Lewis icing research tunnel. In Proceedings of the 30th Aerospace Sciences Meeting and Exhibit, Reno, NV, USA, 6–9 January 1992; p. 647.
33. Potapczuk, M.G. Aircraft Icing Research at NASA Glenn Research Center. *J. Aerosp. Eng.* **2013**, *26*, 260–276. [CrossRef]
34. Cain, G.E.; Yurczyk, R.F.; Belter, D.L.; Chintamani, S.H. *Boeing Research Aerodynamic/Icing Tunnel Capabilities and Calibration*; SAE Technical Paper; SAE International: Warrendale, PA, USA, 1994. [CrossRef]
35. Oleskiw, M.; Hyde, F.; Penna, P. In-flight icing simulation capabilities of NRC's altitude icing wind tunnel. In Proceedings of the 39th Aerospace Sciences Meeting and Exhibit, Reno, NV, USA, 8–11 January 2001.
36. Bansmer, S.E.; Baumert, A.; Sattler, S.; Knop, I.; Leroy, D.; Schwarzenboeck, A.; Jurkat-Witschas, T.; Voigt, C.; Pervier, H.; Esposito, B. Design, construction and commissioning of the Braunschweig Icing Wind Tunnel. *Atmos. Meas. Tech.* **2018**, *11*, 3221–3249. [CrossRef]
37. Hammond, D. Cranfield University Icing Wind Tunnel. In Proceedings of the 41st Aerospace Sciences Meeting and Exhibit, Reno, NV, USA, 6–9 January 2003; p. 901.
38. Vecchione, L.; De Matteis, P. An Overview of the CIRA Icing Wind Tunnel. In Proceedings of the 41st Aerospace Sciences Meeting and Exhibit, Reno, NV, USA, 6–9 January 2003; p. 900.
39. Fengler, M. *Study of Propeller Icing Hazard in Mini-UAV Aviation*; Meteomatics GmbH Technical Report; Meteomatics GmbH: Berlin, Germany, 2017.
40. Kind, R.; Potapczuk, M.; Feo, A.; Golia, C.; Shah, A. Experimental and computational simulation of in-flight icing phenomena. *Prog. Aerosp. Sci.* **1998**, *34*, 257–345. [CrossRef]

41. Messinger, B.L. Equilibrium Temperature of an Unheated Icing Surface as a Function of Air Speed. *J. Aeronaut. Sci.* **1953**, *20*, 29–42. [CrossRef]
42. Wright, W. *User's Manual for LEWICE Version 3.2*; NTRS—NASA Technical Reports Server (NASA/CR—2008-214255 November 2008); NASA Technical Reports Server (NTRS): Cleveland, OH, USA, 2008.
43. Hedde, T.; Guffond, D. ONERA three-dimensional icing model. *AIAA J.* **1995**, *33*, 1038–1045. [CrossRef]
44. Trontin, P.; Kontogiannis, A.; Blanchard, G.; Villedieu, P. Description and assessment of the new ONERA 2D icing suite IGLOO2D. In Proceedings of the 9th AIAA Atmospheric and Space Environments Conference, Denver, CO, USA, 5–9 June 2017. [CrossRef]
45. Mingione, G.; Brandi, V.; Saporiti, A. A 3D ice accretion simulation code. In Proceedings of the 37th Aerospace Sciences Meeting and Exhibit, Reno, NV, USA, 11–14 January 1999; p. 247.
46. Paraschivoiu, I.; Saeed, F. Ice accretion simulation code canice. In Proceedings of the International Areospace Symposium, Bucharest, Romania, 19–20 October 2001; pp. 81–86.
47. Szilder, K.; Lozowski, E.P. Simulation of airfoil icing with a novel morphogenetic model. *J. Aerosp. Eng.* **2005**, *18*, 102–110. [CrossRef]
48. Morency, F.; Beaugendre, H.; Baruzzi, G.; Habashi, W. FENSAP-ICE-A comprehensive 3D simulation system for in-flight icing. In Proceedings of the 15th AIAA Computational Fluid Dynamics Conference, Anaheim, CA, USA, 11–14 June 2001; p. 2566.
49. Tran, P.; Barruzi, G.; Tremblay, F.; Habashi, W.; Petersen, P.; Ligget, M.; Vos, J.; Benquet, P.; Fiorucci, S. FENSAP-ICE applications to unmanned aerial vehicles (UAV). In Proceedings of the 42nd AIAA Aerospace Sciences Meeting and Exhibit, Reno, NV, USA, 5–8 January 2004.
50. Kind, R.J. *Ice Accretion Simulation Evaluation Test (Essai d'evaluation de la simulation de l'accumulation de glace)*; North Atlantic Treaty Organization RTO Technical Rept. TR-038; Nato Research and Technology Organization: Neuilly-Sur-Seine, France, 2001; p. 32.
51. AC-9C Aircraft Icing Technology Committee. *Icing Wind Tunnel Interfacility Comparison Tests*; Aerospace Information Report, AIR5666, SAE Aerospace; SAE International: Warrendale, PA, USA, 2012. [CrossRef]
52. Hann, R. UAV Icing: Comparison of LEWICE and FENSAP-ICE for Ice Accretion and Performance Degradation. In Proceedings of the 2018 Atmospheric and Space Environments Conference, Atlanta, Georgia, 25–29 June 2018.
53. Jeck, R.K. *Icing Design Envelopes (14 CFR Parts 25 and 29, Appendix C) Converted to a Distance-Based*; Federal Aviation Administration, U.S. Department of Transportation: Washington, DC, USA, 2002.
54. Hann, R. UAV Icing: Ice Accretion Experiments and Validation In Proceedings of the International Conference on Icing of Aircraft, Engines, and Structures, Minneapolis, MN, USA, 17–21 June 2019.
55. Hann, R.; Johansen, T.A. UAV icing: The influence of airspeed and chord length on performance degradation. *Aircr. Eng. Aerosp. Technol.* **2021**, *93*, 832–841. [CrossRef]
56. Hann, R. Atmospheric Ice Accretions, Aerodynamic Icing Penalties, and Ice Protection Systems on Unmanned Aerial Vehicles. Ph.D. Thesis, Norwegian University of Science and Technology, Trondheim, Norway, 2020.
57. Hann, R.; Hearst, R.J.; Sætran, L.; Bracchi, T. Experimental and Numerical Icing Penalties of an S826 Airfoil at Low Reynolds Numbers. *Aerospace* **2020**, *7*, 46. [CrossRef]
58. Tummers, M.J.; Steunebrink, M. Effect of surface roughness on heat transfer in Rayleigh-Bénard convection. *Int. J. Heat Mass Transf.* **2019**, *139*, 1056–1064. [CrossRef]
59. Zhang, Y.-Z.; Sun, C.; Bao, Y.; Zhou, Q. How surface roughness reduces heat transport for small roughness heights in turbulent Rayleigh–Bénard convection. *J. Fluid Mech.* **2018**, *836*, R2. [CrossRef]
60. Myers, T.G. Extension to the Messinger Model for Aircraft Icing. *AIAA J.* **2001**, *39*, 211–218. [CrossRef]
61. Dukhan, N.; Va, G., Jr.; Masiulaniec, K.; DeWitt, K. Convective heat transfer coefficients from various types of ice roughened surfaces in parallel and accelerating flow. In Proceedings of the 34th Aerospace Sciences Meeting and Exhibit, Reno, NV, USA, 15–18 January 1996.
62. Henry, R.C.; Guffond, D.; Garnier, F.; Bouveret, A. Heat Transfer Coefficient Measurement on Iced Airfoil in Small Icing Wind Tunnel. *J. Thermophys. Heat Transf.* **2000**, *14*, 348–354. [CrossRef]
63. Koenig, G.; Ryerson, C.; Kmiec, R. UAV icing flight simulation. In Proceedings of the 40th AIAA Aerospace Sciences Meeting & Exhibit, Reno, NV, USA, 14–17 January 2002.
64. Szilder, K.; McIlwain, S. *In-Flight Icing of UAVs—The Influence of Reynolds Number on the Ice Accretion Process*; SAE Technical Paper 2011-01-2572; SAE International: Warrendale, PA, USA, 2011. [CrossRef]
65. Szilder, K.; Yuan, W. The Influence of Ice Accretion on the Aerodynamic Performance of a UAS Airfoil. In Proceedings of the 53rd AIAA Aerospace Sciences Meeting, Kissimmee, FL, USA, 5–9 January 2015. [CrossRef]
66. Szilder, K.; Yuan, W. In-flight icing on unmanned aerial vehicle and its aerodynamic penalties. *Prog. Flight Phys.* **2017**, *9*, 173–188. [CrossRef]
67. Krøgenes, J.; Brandrud, L.; Hann, R.; Bartl, J.; Bracchi, T.; Sætran, L. Aerodynamic Performance of the NREL S826 Airfoil in Icing Conditions. *Wind. Energ. Sci. Discuss.* **2017**, *2017*, 1–17. [CrossRef]
68. Fajt, N.; Hann, R.; Lutz, T. The Influence of Meteorological Conditions on the Icing Performance Penalties on a UAV Airfoil. In Proceedings of the 8th European Conference for Aeronautics and Space Sciences (EUCASS), Madrid, Spain; 2019.
69. Li, H.; Zhang, Y.; Chen, H. Optimization design of airfoils under atmospheric icing conditions for UAV. *Chin. J. Aeronaut.* **2021**, *35*, 118–133. [CrossRef]

70. Cistriani, L. Falco UAV Low Reynolds Airfoil Design and Testing at Galileo Avionica. In *UAV Design Processes/Design Criteria for Structures*; Galileo Avionica Ronchi Dei Legionari (Italy) Simulators and Uav Business Unit; RTO: Neuilly-sur-Seine, France, 2007.
71. Bottyán, Z. In-flight icing characteristics of unmanned aerial vehicles during special atmospheric condition over the Carpathian-basin. *Landsc. Environ.* **2013**, *7*, 74–80.
72. Bottyán, Z. Estimation of in-flight icing characteristics of UAVs during different meteorological conditions. In Proceedings of the 8th International Conference on Intelligent Unmanned Systems (ICIUS 2012), Singapore, 22 October 2012; pp. 418–422.
73. Körpe, D.S.; Yırtıcı, Ö.; Özgen, S. Aerodynamic Performance Losses due to Ice Formation on the UAV's Wings. *J. Aeronaut. Space Technol.* **2020**, *13*, 207–215.
74. Langtry, R.B.; Menter, F. Correlation-Based Transition Modeling for Unstructured Parallelized Computational Fluid Dynamics Codes. *AIAA J.* **2009**, *47*, 2894–2906. [CrossRef]
75. Oswald, J.W.; Enache, A.; Hann, R.; Glabeke, G.; Lutz, T. UAV Icing: Experimental and Numerical Study of Glaze Ice Performance Penalties on an RG-15 Airfoil. In Proceedings of the AIAA Scitech 2022 Forum, San Diego, CA, USA, 3–7 January 2022.
76. Hain, R.; Kähler, C.; Radespiel, R. Dynamics of laminar separation bubbles at low-Reynolds-number aerofoils. *J. Fluid Mech.* **2009**, *630*, 129–153. [CrossRef]
77. Gurbacki, H. Ice-Induced Unsteady Flowfield Effects on Airfoil Performance. Ph.D. Thesis, University of Illinois at Urbana-Champaign, Champaign, IL, USA, 2003.
78. O'Meara, M.M.; Mueller, T.J. Laminar separation bubble characteristics on an airfoil at low Reynolds numbers. *AIAA J.* **1987**, *25*, 1033–1041. [CrossRef]
79. Oo, N.L.; Kay, N.J.; Brenkley, A.J.; Sharma, R.N. Investigation into the behaviour of an iced low Reynolds number aerofoil. In Proceedings of the 10th International Micro-Air Vehicles Conference, Melbourne, Australia, 22–23 November 2018.
80. Garbaruk, A.; Shur, M.; Strelets, M. NACA0021 at 60 deg. incidence. *Notes Numer. Fluid Mech. Multidisiplinary Des.* **2009**, *103*, 127–139.
81. Oo, N.L.; Richards, P.J.; Sharma, R.N. Numerical investigation of clean and ice-accreted aerofoils at low Reynolds number and low angle of attack. In Proceedings of the 21st Australasian Fluid Mechanics Conference, Adelaide, Australia, 10–13 December 2018.
82. Oo, N.L.; Richards, P.J.; Sharma, R.N. Ice-Induced Separation Bubble on RG-15 Airfoil at Low Reynolds Number. *AIAA J.* **2020**, *58*, 5156–5167. [CrossRef]
83. Oo, N.L.; Richards, P.; Sharma, R. Influence of an ice-induced separation bubble on the laminar separation bubble on an RG-15 airfoil at low Reynolds numbers. In Proceedings of the AIAA AVIATION 2020 FORUM, Virtual, 15–19 June 2020. [CrossRef]
84. Huang, R.F.; Lin, C.L. Vortex shedding and shear-layer instability of wing at low-Reynolds numbers. *AIAA J.* **1995**, *33*, 1398–1403. [CrossRef]
85. Bragg, M.B.; Khodadoust, A.; Spring, S.A. Measurements in a leading-edge separation bubble due to a simulated airfoil ice accretion. *AIAA J.* **1992**, *30*, 1462–1467. [CrossRef]
86. Oswald, J.W. UAV Icing: Numerical and Experimental Study of Performance Penalties on an RG-15 Airfoil. Master's Thesis, University of Stuttgart, Stuttgart, Germany, 2021.
87. Li, H.; Zhang, Y.; Chen, H. Aerodynamic Prediction of Iced Airfoils Based on Modified Three-Equation Turbulence Model. *AIAA J.* **2020**, *58*, 3863–3876. [CrossRef]
88. Hann, R. UAV Icing: Comparison of LEWICE and FENSAP-ICE for Anti-Icing Loads. In Proceedings of the AIAA Scitech 2019 Forum, San Diego, CA, USA, 7–11 January 2019.
89. Hann, R.; Wenz, A.; Gryte, K.; Johansen, T. Impact of Atmospheric Icing on UAV Aerodynamic Performance. In Proceedings of the 2017 Workshop on Research, Education and Development of Unmanned Aerial Systems (RED-UAS), Linköping, Sweden, 3–5 October 2017.
90. Gantasala, S. *Flutter Analysis of an Aerofoil Section with Different Ice Shapes at the Leading Edge*; Luleå University of Technology: Luleå, Sweden, 2017.
91. Gantasala, S.; Luneno, J.-C.; Aidanpää, J.-O. Influence of Icing on the Modal Behavior of Wind Turbine Blades. *Energies* **2016**, *9*, 862. [CrossRef]
92. Etemaddar, M.; Hansen, M.; Moan, T. Wind turbine aerodynamic response under atmospheric icing conditions. *Wind. Energy* **2014**, *17*, 241–265. [CrossRef]
93. Thomas, S.K.; Cassoni, R.P.; MacArthur, C.D. Aircraft anti-icing and de-icing techniques and modeling. *J. Aircr.* **1996**, *33*, 841–854. [CrossRef]
94. Botura, G.; Fahrner, A. Icing Detection System—Conception, Development, Testing and Applicability to UAVs. In Proceedings of the 2nd AIAA Unmanned Unlimited Conference and Workshop & Exhibit, San Diego, CA, USA, 15–18 September 2003.
95. Cristofaro, A.; Johansen, T.A.; Aguiar, A.P. Icing detection and identification for unmanned aerial vehicles: Multiple model adaptive estimation. In Proceedings of the 2015 European Control Conference (ECC), Linz, Austria, 15–17 July 2015; pp. 1651–1656.
96. Cristofaro, A.; Johansen, T.A. An unknown input observer approach to icing detection for unmanned aerial vehicles with linearized longitudinal motion. In Proceedings of the 2015 American Control Conference (ACC), Chicago, IL, USA, 1–3 July 2015; pp. 207–213.

97. Rotondo, D.; Cristofaro, A.; Johansen, T.A.; Nejjari, F.; Puig, V. Icing detection in unmanned aerial vehicles with longitudinal motion using an LPV unknown input observer. In Proceedings of the 2015 IEEE Conference on Control Applications (CCA), Sydney, Australia, 21–23 September 2015; pp. 984–989.
98. Seron, M.M.; Johansen, T.A.; Doná, J.A.D.; Cristofaro, A. Detection and estimation of icing in unmanned aerial vehicles using a bank of unknown input observers. In Proceedings of the 2015 5th Australian Control Conference (AUCC), Gold Coast, Australia, 5–6 November 2015; pp. 87–92.
99. Sorensen, K.L.; Blanke, M.; Johansen, T.A. Diagnosis of Wing Icing Through Lift and Drag Coefficient Change Detection for Small. *IFAC-PapersOnLine* **2015**, *48*, 541–546. [CrossRef]
100. Wenz, A.; Johansen, T.A. Icing detection for small fixed wing UAVs using inflight aerodynamic coefficient estimation. In Proceedings of the 2016 IEEE Conference on Control Applications (CCA), Buenos Aires, Argentina, 19–22 September 2016; pp. 230–236.
101. Rotondo, D.; Cristofaro, A.; Hassani, V.; Johansen, T.A. Icing diagnosis in unmanned aerial vehicles using an LPV multiple model estimator. *IFAC-PapersOnLine* **2017**, *50*, 5238–5243. [CrossRef]
102. Wenz, A.; Johansen, T.A. Icing Detection for Small Fixed Wing UAVs using Inflight Aerodynamic Coefficient Estimation. In Proceedings of the 2019 IEEE Aerospace Conference, Big Sky, MT, USA, 2–9 March 2019; pp. 1–9.
103. Haaland, O.M.; Wenz, A.W.; Gryte, K.; Hann, R.; Johansen, T.A. Detection and Isolation of Propeller Icing and Electric Propulsion System Faults in Fixed-Wing UAVs. In Proceedings of the 2021 International Conference on Unmanned Aircraft Systems (ICUAS), Athens, Greece, 15–18 June 2021; pp. 377–386.
104. Energy-Efficient Systems Eliminate Icing Danger for UAVs. Available online: https://spinoff.nasa.gov/Spinoff2010/ps_2.html (accessed on 15 January 2022).
105. Bhakta, B. Novel Ice Protection System Suitable for Unmanned Aerial Vehcile Wing. Ph.D. Thesis, Cranfield University, Cranfield, UK, 2005.
106. Venna, S.V.; Lin, Y.-J.; Botura, G. Piezoelectric Transducer Actuated Leading Edge De-Icing with Simultaneous Shear and Impulse Forces. *J. Aircr.* **2007**, *44*, 509–515. [CrossRef]
107. Ameduri, S.; Guida, D. Investigations on the use of Lamb waves for de-icing purposes. In Proceedings of the ICAST2014: 25nd International Conference on Adaptive Structures and Technologies, The Hague, The Netherlands, 6–8 October 2014.
108. Palacios, J.; Smith, E.; Gao, H.; Rose, J. Ultrasonic Shear Wave Anti-Icing System for Helicopter Rotor Blades. In Proceedings of the American Helicopter Society 62nd Annual Forum, Phoenix, AZ, USA, 9–11 May 2006.
109. Myose, R.Y.; Horn, W.J.; Hwang, Y.; Herrero, J.; Huynh, C.; Boudraa, T. *Application of Shape Memory Alloys for Leading Edge Deicing*; SAE Technical Paper; SAE: Warrendale, PA, USA, 1999. [CrossRef]
110. Buschhorn, S.T.; Kessler, S.S.; Lachmann, N.; Gavin, J.; Thomas, G.; Wardle, B.L. Electrothermal Icing protection of Aerosurfaces Using Conductive Polymer Nanocomposites. In Proceedings of the 54th AIAA/ASME/ASCE/AHS/ASC Structures, Structural Dynamics, and Materials Conference, Boston, MA, USA, 8–11 April 2013.
111. Farcas, C.; Galao, O.; Vertuccio, L.; Guadagno, L.; Romero-Sánchez, M.D.; Rodríguez-Pastor, I.; Garcés, P. Ice-Prevention and De-Icing Capacity of Epoxy Resin Filled with Hybrid Carbon-Nanostructured Forms: Self-Heating by Joule Effect. *Nanomaterials* **2021**, *11*, 2427. [CrossRef]
112. Redondo, O.; Prolongo, S.G.; Campo, M.; Sbarufatti, C.; Giglio, M. Anti-icing and de-icing coatings based Joule's heating of graphene nanoplatelets. *Compos. Sci. Technol.* **2018**, *164*, 65–73. [CrossRef]
113. Guadagno, L.; Foglia, F.; Pantani, R.; Romero-Sanchez, M.D.; Calderón, B.; Vertuccio, L. Low-Voltage Icing Protection Film for Automotive and Aeronautical Industries. *Nanomaterials* **2020**, *10*, 1343. [CrossRef]
114. Vertuccio, L.; Foglia, F.; Pantani, R.; Romero-Sánchez, M.D.; Calderón, B.; Guadagno, L. Carbon nanotubes and expanded graphite based bulk nanocomposites for de-icing applications. *Compos. Part B Eng.* **2021**, *207*, 108583. [CrossRef]
115. Idris, M.K.; Qiu, J.; Melenka, G.W.; Grau, G. Printing electronics directly onto carbon fiber composites: Unmanned aerial vehicle (UAV) wings with integrated heater for de-icing. *Eng. Res. Express* **2020**, *2*, 025022. [CrossRef]
116. Sorensen, K.; Helland, A.; Johansen, T. Carbon nanomaterial-based wing temperature control system for in-flight anti-icing and de-icing of unmanned aerial vehicles. In Proceedings of the IEEE Aerospace Conference Proceedings, Big Sky, MT, USA, 7–14 March 2015. [CrossRef]
117. KimLynge Sørensen, T.A.J. Thermodynamics of a Carbon Nano-Materials Based Icing Protection System for Unmanned Aerial Vehicle. In Proceedings of the IEEE Aerospace Conference, Big Sky, MT, USA, 5–12 March 2016.
118. S⊘rensen, K.L.; Johansen, T.A. Flight test results for autonomous icing protection solution for small unmanned aircraft. In Proceedings of the 2017 International Conference on Unmanned Aircraft Systems (ICUAS), Miami, FL, USA, 13–16 June 2017; pp. 971–980.
119. Hwang, H.; Ma, K.Y.; Kim, J.W.; Yuk, D.; Hong, J.; Jung, J.H.; Yong, S.-M.; Choi, J.; Kim, J.Y.; Shin, H.S. Radio-frequency-transmitting hexagonal boron nitride-based anti- and de-icing heating system. *Nanoscale* **2020**, *12*, 21895–21900. [CrossRef]
120. Hann, R.; Enache, A.; Nielsen, M.C.; Stovner, B.N.; van Beeck, J.; Johansen, T.A.; Borup, K.T. Experimental Heat Loads for Electrothermal Anti-Icing and De-Icing on UAVs. *Aerospace* **2021**, *8*, 83. [CrossRef]
121. Bhushan, B.; Chae Jung, Y. Wetting study of patterned surfaces for superhydrophobicity. *Ultramicroscopy* **2007**, *107*, 1033–1041. [CrossRef] [PubMed]

122. Michael, N.; Bhushan, B. Hierarchical roughness makes superhydrophobic states stable. *Microelectron. Eng.* **2007**, *84*, 382–386. [CrossRef]
123. Nosonovsky, M.; Bhushan, B. Roughness-induced superhydrophobicity: A way to design non-adhesive surfaces. *J. Phys. Condens. Matter* **2008**, *20*, 225009. [CrossRef]
124. Nosonovsky, M.; Bhushan, B. Patterned Nonadhesive Surfaces: Superhydrophobicity and Wetting Regime Transitions. *Langmuir* **2008**, *24*, 1525–1533. [CrossRef]
125. Farhadi, S.; Farzaneh, M.; Kulinich, S.A. Anti-icing performance of superhydrophobic surfaces. *Appl. Surf. Sci.* **2011**, *257*, 6264–6269. [CrossRef]
126. Farzaneh, M.; Ryerson, C. Anti-icing and deicing techniques. *Cold Reg. Sci. Technol.* **2011**, *65*, 88–96. [CrossRef]
127. Kulinich, S.; Farzaneh, M. How Wetting Hysteresis Influences Ice Adhesion Strength on Superhydrophobic Surfaces. *Langmuir ACS J. Surf. Colloids* **2009**, *25*, 8854–8856. [CrossRef]
128. Kulinich, S.A.; Farzaneh, M. Ice adhesion on super-hydrophobic surfaces. *Appl. Surf. Sci.* **2009**, *255*, 8153–8157. [CrossRef]
129. Kulinich, S.A.; Farzaneh, M. Effect of contact angle hysteresis on water droplet evaporation from super-hydrophobic surfaces. *Appl. Surf. Sci.* **2009**, *255*, 4056–4060. [CrossRef]
130. Wang, F.; Li, C.; Lv, Y.; Lv, F.; Du, Y. Ice accretion on superhydrophobic aluminum surfaces under low-temperature conditions. *Cold Reg. Sci. Technol.* **2010**, *62*, 29–33. [CrossRef]
131. Piscitelli, F.; Chiariello, A.; Dabkowski, D.; Corraro, G.; Marra, F.; Di Palma, L. Superhydrophobic Coatings as Anti-Icing Systems for Small Aircraft. *Aerospace* **2020**, *7*, 2. [CrossRef]